

Correlation driven near-flat band Stoner excitations in a Kagome magnet

Abhishek Nag^{1,*}, Yiran Peng², Jiemin Li^{1,3}, S. Agrestini¹, H. C. Roberts^{1,4}, Mirian García-Fernández¹, A. C. Walters¹, Qi Wang⁵, Qiangwei Yin⁵, Hechang Lei⁵, Zhiping Yin^{2,†}, and Ke-Jin Zhou^{1,‡}

¹Diamond Light Source, Harwell Campus, Didcot OX11 0DE, United Kingdom

²Department of Physics and Center for Advanced Quantum Studies, Beijing Normal University, Beijing 100875, China

³Beijing National Laboratory for Condensed Matter Physics and Institute of Physics, Chinese Academy of Sciences, Beijing 100190, China

⁴H. H. Wills Physics Laboratory, University of Bristol, Bristol BS8 1TL, United Kingdom

⁵Department of Physics and Beijing Key Laboratory of Opto-Electronic Functional Materials & Micro-Nano Devices, Renmin University of China, Beijing 100872, China

*e-mail: abhishek.nag@diamond.ac.uk

†e-mail: yinzhiping@bnu.edu.cn

‡e-mail: kejin.zhou@diamond.ac.uk

ABSTRACT

Among condensed matter systems, Mott insulators exhibit diverse properties that emerge from electronic correlations. In itinerant metals, correlations are usually weak, but can also be enhanced via geometrical confinement of electrons, that manifest as ‘flat’ dispersionless electronic bands. In the fast developing field of topological materials, which includes Dirac and Weyl semimetals, flat bands are one of the important components that can result in unusual magnetic and transport behaviour. To date, characterisation of flat bands and their magnetism is scarce, hindering the design of novel materials. Here, we investigate the ferromagnetic Kagomé semimetal $\text{Co}_3\text{Sn}_2\text{S}_2$ using resonant inelastic X-ray scattering. Remarkably, nearly non-dispersive Stoner spin excitation peaks are observed, sharply contrasting with the featureless Stoner continuum expected in conventional ferromagnetic metals. Our band structure and dynamic spin susceptibility calculations, and thermal evolution of the excitations, confirm the nearly non-dispersive Stoner excitations as unique signatures of correlations and spin-polarized electronic flat bands in $\text{Co}_3\text{Sn}_2\text{S}_2$. These observations serve as a cornerstone for further exploration of band-induced symmetry-breaking orders in topological materials.

Introduction

Over the last few decades, there has been an increasing interest in quantum materials with topological electronic band properties¹. Here, the competition between the Coulomb interaction, Hund's exchange, crystal-field effects, and spin-orbit coupling creates a rich phase space of topologically non-trivial states. These systems including topological insulators, Dirac and Weyl semimetals, display remarkable transport properties when topological bands are tuned to the chemical potential²⁻⁵. In addition to the highly dispersing Dirac and Weyl bands, another class of bands has also drawn much attention. These bands, flat in momentum space, emerge in special lattices owing to geometrically destructive quantum phase interference of electron hopping pathways. Consequently, the electronic kinetic energy gets suppressed, enhancing electronic interactions. Flat band systems can show diverse many-body phenomena like the fractional quantum Hall effect⁶, Mott-insulation⁷ and unconventional superconductivity⁸. Combining with magnetism, topological band systems can serve towards energy-efficient spintronics⁹, as exemplified by the observation of a giant intrinsic anomalous Hall effect in magnetic Weyl semimetals^{10,11}.

Among the solid state systems, Kagomé lattices are the most promising candidates for flat bands. From simple nearest-neighbor tight-binding model considerations, Kagomé lattices may show the presence of both Dirac and flat bands¹². Moreover, Kagomé materials like twisted bilayer graphene and Fe_3Sn_2 have been proposed to host flat band ferromagnetism^{6,13,14}. However, the presence of flat bands is not the sole aspect governing bulk magnetic properties in real materials¹⁴⁻¹⁹. For example, topological flat bands were revealed in frustrated Kagomé metal CoSn by angle-resolved photoemission spectroscopy (ARPES), however, it is a paramagnet^{17,20}. On the other hand, in Kagomé metal $\text{Co}_3\text{Sn}_2\text{S}_2$, although scanning tunnelling spectroscopy (STS)^{15,17} has indicated presence of flat bands in a limited momentum (q)-space, it is nevertheless a ferromagnet with a T_C of $\simeq 175$ K¹⁹. In fact, $\text{Co}_3\text{Sn}_2\text{S}_2$ is one of the few Kagomé systems that are expected to have flat bands and are also ferromagnets. Also, being a Weyl semimetal, $\text{Co}_3\text{Sn}_2\text{S}_2$ promises tunability of its topological properties via magnetism^{10,11,21,22}. To progress the field of band topology driven magnetism, it is therefore crucial to study the flat band magnetic excitations in these materials. This naturally leads to the search for a technique in complement to ARPES and STS, which is sensitive to not only low energy collective spin-waves but also band selective magnetic excitations, like resonant inelastic X-ray scattering (RIXS), owing to the presence of an intermediate core-hole state with strong spin-orbit coupling²³.

Here, we investigate the magnetic excitations from flat bands in $\text{Co}_3\text{Sn}_2\text{S}_2$ using Co L_3 -edge RIXS. We observe a damped excitation peak close to 0.38 eV that has a peak dispersion bandwidth of about 0.05 eV in the probed q -space. We calculate the electronic band structure and vertex corrected dynamic spin structure factor $[S(q, \omega)]$ of $\text{Co}_3\text{Sn}_2\text{S}_2$ using a combination of density functional theory and dynamical mean field theory (DFT+DMFT). The calculated $S(q, \omega)$ show an energy (E)- q -dependence very similar to that in the experiments. Additionally, the comparison of our temperature (T)-dependent results to the calculated $S(q, \omega)$ for the ferromagnetic (FM) and paramagnetic (PM) states allows us to associate the experimentally observed peaks to Stoner excitations. We

thus identify the nearly non-dispersive Stoner excitation peaks as a unique feature of magnetic excitations from correlated electronic flat bands in $\text{Co}_3\text{Sn}_2\text{S}_2$, in stark contrast to conventional FM metals. Our work also serves as the first experimental $E - q$ -space evidence for the presence of flat bands in this system.

Results

In $\text{Co}_3\text{Sn}_2\text{S}_2$, the Co atoms are arranged as stacked layers of Kagomé units as shown in Fig. 1a. It is an itinerant system with a charge carrier density of $1.22 \times 10^{21} \text{ cm}^{-3}$, and a magnetic moment of 0.2-0.3 $\mu\text{B}/\text{Co}$, much smaller than that expected from a local moment scenario^{19,24}. Comparable resonant energy positions of the Co L_3 X-ray absorption (XAS) on $\text{Co}_3\text{Sn}_2\text{S}_2$ with that of Co metal and CoO (Fig. 1b), suggest a d^7 electronic configuration of the Co atoms²⁴. The spin and orbital momentum of the poorly screened core-hole potential couples with the valence d electrons to give rise to multiplet features in a L_3 -XAS process, and are indicative of correlation and local crystal-field strengths²⁵. While at the strong correlation limit the charge-transfer insulator CoO with Hubbard $U = 5.1 \text{ eV}$ ²⁶, shows multiplet fine-structures, at the other extreme, the metallic Co has a featureless asymmetric peak. We note that the XAS of $\text{Co}_3\text{Sn}_2\text{S}_2$ has features qualitatively between the two, indicating an intermediate electronic correlation.

In strongly correlated systems like cuprates or nickelates, excitonic peaks are observed in RIXS from spin, charge, lattice or orbital excitations²³. Although, strong fluorescence signals from delocalised states usually dominate the RIXS signals in itinerant systems, collective spin-waves have been successfully probed, for instance, in iron-based superconductors or Fe and Ni metals²⁷⁻³⁰. The RIXS response of $\text{Co}_3\text{Sn}_2\text{S}_2$ shown in Fig. 1 (c and d), also has a strong fluorescence signal linearly dependent on incident energy (E_i) above the Co L_3 -XAS threshold. However, we observe an additional broad but intense peak close to 0.38 eV which remains fairly independent of E_i . This shows that the peak results from a coherent excitonic process and provides further proof of moderate electronic correlations despite the itinerancy of the system¹⁸. At $E_i = 779.85 \text{ eV}$ where the broad peak (S1) at 0.38 eV is most intense, a high energy resolution RIXS spectrum also reveals a low energy peak (S2) close to 0.04 eV. Spin-wave excitations in $\text{Co}_3\text{Sn}_2\text{S}_2$ have been observed using inelastic neutron scattering (INS) up to 0.018 eV³¹, and as such cannot be resolved from the elastic peak at zero energy with the present energy resolution.

In Fig. 2a and b we present the spin-resolved d -orbital electronic bands in the FM state calculated with $U = 5.0 \text{ eV}$ and Hund's exchange $J_H = 0.9 \text{ eV}$, showing the presence of dispersing as well as flat bands in $\text{Co}_3\text{Sn}_2\text{S}_2$. The overall low-energy band dispersions and energies are in good agreement with reported ARPES data on $\text{Co}_3\text{Sn}_2\text{S}_2$ (see Methods)^{22,32}. Along with the spin-waves, electron-hole pair excitations with electrons and holes in the bands of opposite spins are also elementary to itinerant ferromagnets, and are called the Stoner excitations. The distribution of Stoner excitations in the $E - q$ -space, however, is strongly influenced by the band structure. In conventional ferromagnetic metals with highly dispersing bands, the Stoner excitations are typically spread over several eVs as a

continuum (Fig. 2c, d). The continuum presents no peak-like feature in INS or RIXS experiments and manifests as damping or renormalisation of spin-wave energies for overlapping $E - q$ values²⁹. While in the itinerant flat band ferromagnets, the spin wave energies are expected to maintain qualitatively similar dispersion behaviour (albeit with possible energy renormalisation) as in ordinary itinerant ferromagnets^{33–35}, flattening of the bands confine the spectral weight distribution of the Stoner continuum to a narrow region of the $E - q$ space (Fig. 2c, d)^{33–35}. Stoner excitations across segments of flat bands as shown in Fig. 2a, b and e²³, may appear in Co L -edge RIXS and give rise to the S1 peak in $\text{Co}_3\text{Sn}_2\text{S}_2$, and therefore, next we investigate its dependence in the $E - q$ -space.

Fig. 3a and b show the low-energy RIXS spectra from $\text{Co}_3\text{Sn}_2\text{S}_2$ along the $\bar{\Gamma}\bar{M}$ and $\bar{\Gamma}\bar{A}$ directions. Panels c and d show the corresponding intensity maps with the quasielastic and background contributions subtracted, thereby, highlighting the S1 and S2 peaks. The S1 peaks were fitted with a generic damped harmonic oscillator model having undamped peak energy ω_0 and peak damping factor γ/ω_0 (Fig. 1e and Methods). The largest value of ω_0 for S1 is found to be 0.4 eV. The ω_0 s of the S2 peaks were kept fixed at 0.04 eV as extracted from high energy resolution RIXS spectra (see Methods and Supplementary Information Fig. S5 and S6 showing the non-dispersing S2 peaks). The effect of correlations in the two-particle response functions are generally taken into account following a vertex correction³⁶. For example, the dynamic spin susceptibility $[\chi(q, \omega)]$ is related to the bare spin susceptibility $[\chi_0(q, \omega)]$ as $\chi(q, \omega) = \chi_0(q, \omega)/[1 - \Gamma_V(\omega)\chi_0(q, \omega)]$, where Γ_V is the two-particle vertex function. For weak or uncorrelated itinerant systems, the dynamic spin susceptibility resembles the bare susceptibility owing to a small or zero vertex correction. For correlated systems, a significant renormalisation of spectral shape occurs as $\Gamma_V(\omega)\text{Re } \chi_0(q, \omega)$ values approach 1 giving rise to the poles in $\chi(q, \omega)$. We calculated the bare spin and charge susceptibilities, *i.e.*, the electron-hole pair excitations, based on the DFT+DMFT band structure results with the inclusion of the screened Coulomb interaction and found that both the bare susceptibilities are featureless in the energy range of S1, and have no spectral weight in the energy range of S2 (see Methods and Supplementary Information Fig. S7). Fig. 3e and f show the dynamic structure factor $S(q, \omega) = \text{Im } \chi(q, \omega)/(1 - e^{-\hbar\omega/k_B T})$, obtained after vertex correction (see Methods). The remarkable similarity in the energy scales and the dispersions of S1 (S2) peaks between the experiment and the calculated $S(q, \omega)$, suggests their origin from the spin-flip Stoner excitations in $\text{Co}_3\text{Sn}_2\text{S}_2$, owing to schematically shown $U_1 \rightarrow D_2$ or $D_1 \rightarrow U_3$ ($U_2 \rightarrow D_2$)-like transitions in Fig 2e. At the same time, the significant difference between bare and vertex corrected susceptibilities (see Supplementary Information Fig. S7), underlines the importance of the correlations effects in both the ground state and the collective excitations. We also note that the experimental distributions are distinct to the vertex corrected dynamic charge susceptibilities representing non-spin-flip charge excitations as shown in Fig. 3g and h. In optical studies of $\text{Co}_3\text{Sn}_2\text{S}_2$, a peak close to 0.2 eV was observed in the FM state, which gradually broadened in the PM state and was assigned to non-spin-flip excitations from the flat bands¹⁶. Our charge susceptibility calculations are consistent with the optical result. While spin-conserved processes are also allowed in RIXS, we do not observe any additional peak-like feature in the almost linear RIXS

spectra between 0.1 – 0.38 eV¹⁶. We thus refrain from performing a multi-component fitting of S1 and report the single component ω_0 and γ/ω_0 in this work. The potential contribution of the charge susceptibility could be the reason behind the large damping ($\gamma/\omega_0 \approx 0.5$), observed for S1 compared to the calculations. Similarly, while the energy scale of S2 matches with the low energy component of calculated spin-susceptibility, we cannot discard optical phonon contributions at this energy¹⁸. A quantitative estimation of these contributions to the effective RIXS scattering cross-section is however, beyond the capabilities of presently available computational methods.

To further demonstrate the dominant contribution of Stoner excitations to the S1 peaks, we collected temperature dependent RIXS spectra across the T_C of $\text{Co}_3\text{Sn}_2\text{S}_2$. As shown in Fig. 4a, the peak height of S1 with $\omega_0 \simeq 0.38$ eV, decreases till the T_C , above which it becomes featureless and shows almost no change till 347 K in the PM state. In Fig. 4b, we present the temperature dependent RIXS intensity map along with ω_0 of S1 extracted from fitting. We observe clearly the spectral weight shift along with the change in ω_0 below and above T_C . Such a shift and loss in the peak height seen in Fig. 4a, is expected because the bands become partially non-spin-polarised and shift in energy above T_C (see Supplementary information Fig. S8)³². This is also reflected in the concomitant shift towards higher energy in the calculated $S(q, \omega)$ in the PM state (Fig. 4c and Supplementary Information Fig. S8). Similarly, for paramagnetic CoSn which does not have spin-polarised bands, Co L_3 -edge RIXS collected at 20 K is devoid of any peak-like feature in this region, as shown in Fig. 4a (see also Supplementary Information Fig. S9). It was shown in Ref.¹⁹, that $\text{Co}_3\text{Sn}_2\text{S}_2$ exhibits a c -axis FM ground state until $T_C^* \approx 90$ K, above which an additional ab -plane antiferromagnetic component starts growing, eventually attaining a volume fraction of 80% at $\simeq 170$ K and finally becoming PM above T_C . From Fig. 4b and d, we observe that the ω_0 and γ/ω_0 remain nearly constant below T_C^* , and starts rising linearly with the reduction in the FM volume fraction. Above T_C , when the system becomes PM, ω_0 again stops changing, along with the decline in the rate of change of damping. In itinerant ferromagnets the band structure evolves continuously with temperature and our results show that the observed excitations are intricately linked to the magnetism in $\text{Co}_3\text{Sn}_2\text{S}_2$. Since we observe spectral weights, although largely damped, till almost twice the T_C , this indicates that the magnetic moment fluctuations and electronic correlations persist much above T_C , also suggested by Rossi et al. in their recent work on $\text{Co}_3\text{Sn}_2\text{S}_2$ ³⁷.

Discussions

While $\text{Co}_3\text{Sn}_2\text{S}_2$ has attracted a lot of interest in recent years due to its topological properties and magnetism, there has been no momentum resolved experimental evidence of flat bands in this system^{15,18}. We have demonstrated with the observation of Stoner excitation peaks with a dispersion bandwidth of about 0.05 eV over 65% of a Brillouin zone in the $\bar{\Gamma}-\bar{M}$ direction, the presence of flat bands in this system. It should be highlighted that the dispersion bandwidth estimated from the Stoner excitations has the combined contribution of both the valence and conduction bands, as well as the q -dependent exchange splitting energy, and therefore can serve as a more stringent test

for the existence of flat bands. The Stoner excitation peaks also have a dispersion bandwidth of about 0.05 eV along the out-of-plane direction suggesting presence of interlayer electron interactions and deviation from ideal two dimensionality in this system³⁸.

The excitations observed in the experiments are not particle hole excitations from the joint density of states as demonstrated by the absence of peak like features in the calculated bare spin/charge susceptibilities at the energy scales of S1 and S2 peaks. The resemblance in the energy scales and dispersion between the experiments and the vertex corrected dynamic spin susceptibilities show the importance of correlations driving the two-particle spin response or the Stoner excitations from the flat bands in this system. Furthermore, the excitations are intricately linked to the thermal evolution of the electronic bands and the associated magnetism.

The low energy excitations are crucial to understand the interaction-driven many-body ground states governing the material properties when the bands are tuned to the chemical potential. While ARPES is the choice tool to investigate the valence bands our results demonstrate that RIXS can be utilised for identifying the presence of flat bands and the energy scales in both valence and conduction bands, providing information that may be utilised to modify the electronic/magnetic properties of these materials by doping. Direct experimental observation of Stoner excitations in RIXS also means that it can be used to clarify the magnon-Stoner interactions in itinerant correlated flat band systems like FeSn where INS have observed discrepancies in magnon intensities at energies relevant to Stoner excitations³⁹.

Methods

Sample details

$\text{Co}_3\text{Sn}_2\text{S}_2$ single crystals were grown by the Sn flux method. The starting elements of Co (99.99 %), Sn (99.99 %) and S (99.99 %) were put into an alumina crucible, with a molar ratio of Co : S : Sn = 4 : 3 : 43. The mixture was sealed in a quartz ampoule under partial argon atmosphere and heated up to 1323 K, then cooled down to 973 K at 5 K/h. The $\text{Co}_3\text{Sn}_2\text{S}_2$ single crystals were separated from the Sn flux by using centrifuge. FM transition temperature T_C from magnetisation measurements was found to be 172 K. See Supplementary Information for sample characterisation details.

Theoretical calculations

A combination of density functional theory and dynamical mean field theory (DFT+DMFT)⁴⁰ were used to compute the electronic band structure of $\text{Co}_3\text{Sn}_2\text{S}_2$ in the FM and PM states (see Supplementary information Fig. S10). The full-potential linear augmented plane wave method implemented in Wien2K⁴¹ was used for the DFT part. The Perdew–Burke–Ernzerhof type generalized gradient approximation⁴² was used for the exchange correlation functional. DFT+DMFT was implemented on top of Wien2K which is described in detail in Ref.⁴³. In the DFT+DMFT calculations, the electronic charge was computed self-consistently on DFT+DMFT density matrix. The quantum

impurity problem was solved by the continuous time quantum Monte Carlo (CTQMC) method^{44,45} with $U = 5.0$ eV and Hund's exchange $J_H = 0.9$ eV in both FM and PM states. Bethe-Salpeter equation was used to compute the dynamic spin susceptibility where the bare susceptibility was computed using the converged DFT+DMFT Green's function, while the two-particle vertex was directly sampled using CTQMC method after achieving full self-consistency of DFT+DMFT density matrix³⁶. For the FM state, the averaged Green's function of the spin-up and spin-down channels was used to compute the bare susceptibility. The experimental crystal structure (space group $R\bar{3}m$, No. 166) of $\text{Co}_3\text{Sn}_2\text{S}_2$ with hexagonal lattice constants $a = b = 5.3689$ Å and $c = 13.176$ Å was used in the calculations.

RIXS measurements

The Co L_3 -edge XAS spectra shown in Fig. 1b was collected in total electron yield mode using σ -polarised X-ray. Momentum transfer $q = ha^* + kb^* + lc^*$ is defined using Miller indices (h, k, l) in reciprocal lattice units. We state the values of (h, l) and $k = 0$ if not stated explicitly. Crystals were cleaved in vacuum and the pressure in the experimental chamber was maintained below 5×10^{-10} mbar. RIXS spectra presented at Co L_3 -edge were collected with an energy resolution of $\Delta E \simeq 0.048$ eV, at I21-RIXS beam line, Diamond Light Source, United Kingdom⁴⁶. Additional spectra were also collected with $\Delta E \simeq 0.032$ eV. Samples were mounted such that the c -axis was in the horizontal scattering plane (Fig. 1a). While the E_i dependent RIXS spectra were collected using π -polarised X-ray, the q and T dependent RIXS spectra were collected using σ -polarised X-ray. The zero-energy transfer position and resolution of the RIXS spectra were determined from subsequent measurements of elastic peaks from an amorphous carbon sample.

RIXS data fitting

RIXS data were normalised to the incident photon flux, and subsequently corrected for self-absorption effects, prior to fitting. A Gaussian lineshape with the experimental energy resolution was used to fit the quasielastic line. A high energy Gaussian background was included in the fitting model to account for the contribution from fluorescence features. The scattering intensities $S(\mathbf{q}, \omega)$ of peaks S1 and S2 were modelled using a generic damped harmonic oscillator function:

$$S(\mathbf{q}, \omega) \propto \frac{1}{1 - e^{-\hbar\omega/k_B T}} \frac{\gamma\omega}{[\omega^2 - \omega_0^2]^2 + 4\omega^2\gamma^2}, \quad (1)$$

where k_B , T and \hbar are the Boltzmann constant, temperature and the reduced Planck constant. ω_0 and γ are the undamped frequency and the damping factor of the peaks, respectively. The peak is underdamped if $\gamma/\omega_0 < 1$. See Supplementary Information Fig. S2-S4 showing the fitting profiles. Since the S2 peak cannot be resolved from the quasielastic peak in the spectra with $\Delta E \simeq 0.048$ eV, the S2 peak positions (0.04 eV) were determined from the spectra collected with $\Delta E \simeq 0.032$ eV and fixed for the lower resolution scans (Supplementary Information Fig. S5

and S6).

Data availability

The experimental data presented in the figures are available as a public data set at <https://doi.org/10.5281/zenodo.7264820>.

Code availability

The codes used for the DFT+DMFT calculations in this study are available from the corresponding authors upon reasonable request.

References

1. Witczak-Krempa, W., Chen, G., Kim, Y. B. & Balents, L. Correlated quantum phenomena in the strong spin-orbit regime. *Annu. Rev. Condens. Matter Phys.* **5**, 57–82 (2014).
2. Hasan, M. Z., Xu, S.-Y. & Bian, G. Topological insulators, topological superconductors and Weyl fermion semimetals: discoveries, perspectives and outlooks. *Phys. Scr.* **T164**, 014001 (2015).
3. He, K., Wang, Y. & Xue, Q.-K. Topological materials: quantum anomalous Hall System. *Annu. Rev. Condens. Matter Phys.* **9**, 329–344 (2018).
4. Armitage, N. P., Mele, E. J. & Vishwanath, A. Weyl and Dirac semimetals in three-dimensional solids. *Rev. Mod. Phys.* **90**, 015001 (2018).
5. Burkov, A. Weyl metals. *Annu. Rev. Condens. Matter Phys.* **9**, 359–378 (2018).
6. Sun, K., Gu, Z., Katsura, H. & Das Sarma, S. Nearly flatbands with nontrivial topology. *Phys. Rev. Lett.* **106**, 236803 (2011).
7. Cao, Y. *et al.* Correlated insulator behaviour at half-filling in magic-angle graphene superlattices. *Nature* **556**, 80–84 (2018).
8. Chen, G. *et al.* Signatures of tunable superconductivity in a trilayer graphene moiré superlattice. *Nature* **572**, 215–219 (2019).
9. Wang, X. S., Zhang, H. W. & Wang, X. R. Topological magnonics: A paradigm for spin-wave manipulation and device design. *Phys. Rev. Appl.* **9**, 024029 (2018).
10. Liu, E. *et al.* Giant anomalous Hall effect in a ferromagnetic kagome-lattice semimetal. *Nat. Phys.* **14**, 1125–1131 (2018).
11. Wang, Q. *et al.* Large intrinsic anomalous Hall effect in half-metallic ferromagnet $\text{Co}_3\text{Sn}_2\text{S}_2$ with magnetic Weyl fermions. *Nat. Commun.* **9**, 3681 (2018).

12. Mazin, I. I. *et al.* Theoretical prediction of a strongly correlated dirac metal. *Nat. Commun.* **5**, 4261 (2014).
13. Lopez-Bezanilla, A. Emergence of flat-band magnetism and half-metallicity in twisted bilayer graphene. *Phys. Rev. Mater.* **3**, 054003 (2019).
14. Lin, Z. *et al.* Flatbands and emergent ferromagnetic ordering in Fe₃Sn₂ Kagome lattices. *Phys. Rev. Lett.* **121**, 096401 (2018).
15. Yin, J.-X. *et al.* Negative flat band magnetism in a spin–orbit-coupled correlated kagome magnet. *Nat. Phys.* **15**, 443–448 (2019).
16. Yang, R. *et al.* Magnetization-induced band shift in ferromagnetic Weyl semimetal Co₃Sn₂S₂. *Phys. Rev. Lett.* **124**, 077403 (2020).
17. Kang, M. *et al.* Topological flat bands in frustrated kagome lattice CoSn. *Nat. Commun.* **11**, 4004 (2020).
18. Xu, Y. *et al.* Electronic correlations and flattened band in magnetic Weyl semimetal candidate Co₃Sn₂S₂. *Nat. Commun.* **11**, 3985 (2020).
19. Guguchia, Z. *et al.* Tunable anomalous Hall conductivity through volume-wise magnetic competition in a topological kagome magnet. *Nat. Commun.* **11**, 559 (2020).
20. Liu, Z. *et al.* Orbital-selective Dirac fermions and extremely flat bands in frustrated kagome-lattice metal CoSn. *Nat. Commun.* **11**, 4002 (2020).
21. Morali, N. *et al.* Fermi-arc diversity on surface terminations of the magnetic weyl semimetal Co₃Sn₂S₂. *Science* **365**, 1286–1291 (2019).
22. Liu, D. F. *et al.* Magnetic Weyl semimetal phase in a Kagomé crystal. *Science* **365**, 1282–1285 (2019).
23. Ament, L. J. P., van Veenendaal, M., Devereaux, T. P., Hill, J. P. & van den Brink, J. Resonant inelastic x-ray scattering studies of elementary excitations. *Rev. Mod. Phys.* **83**, 705–767 (2011).
24. Li, G. *et al.* Surface states in bulk single crystal of topological semimetal Co₃Sn₂S₂ toward water oxidation. *Sci. Adv.* **5** (2019).
25. de Groot, F. Multiplet effects in X-ray spectroscopy. *Coord. Chem. Rev.* **249**, 31–63 (2005).
26. Jiang, H., Gomez-Abal, R. I., Rinke, P. & Scheffler, M. First-principles modeling of localized d states with the GW LDA + U approach. *Phys. Rev. B* **82**, 045108 (2010).
27. Gilmore, K. *et al.* Description of resonant inelastic x-ray scattering in correlated metals. *Phys. Rev. X* **11**, 031013 (2021).
28. Zhou, K.-J. *et al.* Persistent high-energy spin excitations in iron-pnictide superconductors. *Nat. Commun.* **4**, 1470 (2013).

29. Brookes, N. B. *et al.* Spin waves in metallic iron and nickel measured by soft x-ray resonant inelastic scattering. *Phys. Rev. B* **102**, 064412 (2020).
30. Pellicciari, J. *et al.* Tuning spin excitations in magnetic films by confinement. *Nat. Mater.* **20**, 188–193 (2021).
31. Liu, C. *et al.* Spin excitations and spin wave gap in the ferromagnetic Weyl semimetal $\text{Co}_3\text{Sn}_2\text{S}_2$. *Sci. China Phys. Mech. Astron.* **64**, 217062 (2020).
32. Liu, D. F. *et al.* Topological phase transition in a magnetic weyl semimetal. *Phys. Rev. B* **104**, 205140 (2021).
33. Su, X.-F., Gu, Z.-L., Dong, Z.-Y. & Li, J.-X. Topological magnons in a one-dimensional itinerant flatband ferromagnet. *Phys. Rev. B* **97**, 245111 (2018).
34. Su, X.-F., Gu, Z.-L., Dong, Z.-Y., Yu, S.-L. & Li, J.-X. Ferromagnetism and spin excitations in topological Hubbard models with a flat band. *Phys. Rev. B* **99**, 014407 (2019).
35. Kusakabe, K. & Aoki, H. Ferromagnetic spin-wave theory in the multiband Hubbard model having a flat band. *Phys. Rev. Lett.* **72**, 144–147 (1994).
36. Yin, Z. P., Haule, K. & Kotliar, G. Spin dynamics and orbital-antiphase pairing symmetry in iron-based superconductors. *Nat. Phys.* **10**, 845–850 (2014).
37. Rossi, A. *et al.* Electronic structure and topology across T_c in the magnetic weyl semimetal $\text{Co}_3\text{Sn}_2\text{S}_2$. *Phys. Rev. B* **104**, 155115 (2021).
38. Luo, W., Nakamura, Y., Park, J. & Yoon, M. Cobalt-based magnetic weyl semimetals with high-thermodynamic stabilities. *npj Comput. Mater.* **7**, 2 (2021).
39. Do, S.-H. *et al.* Damped dirac magnon in the metallic kagome antiferromagnet FeSn . *Phys. Rev. B* **105**, L180403 (2022).
40. Kotliar, G. *et al.* Electronic structure calculations with dynamical mean-field theory. *Rev. Mod. Phys.* **78**, 865–951 (2006).
41. Blaha, P., Schwarz, K., Madsen, G. K. H., Kvasnicka, D. & Luitz, J. Wien2k, An Augmented Plane Wave+Local Orbitals Program for Calculating Crystal Properties (Schwarz K., Techn. Universität Wien, 2001).
42. Perdew, J. P., Burke, K. & Ernzerhof, M. Generalized gradient approximation made simple. *Phys. Rev. Lett.* **77**, 3865–3868 (1996).
43. Haule, K., Yee, C.-H. & Kim, K. Dynamical mean-field theory within the full-potential methods: Electronic structure of CeIrIn_5 , CeCoIn_5 , and CeRhIn_5 . *Phys. Rev. B* **81**, 195107 (2010).
44. Haule, K. Quantum monte carlo impurity solver for cluster dynamical mean-field theory and electronic structure calculations with adjustable cluster base. *Phys. Rev. B* **75**, 155113 (2007).

45. Werner, P., Comanac, A., de' Medici, L., Troyer, M. & Millis, A. J. Continuous-time solver for quantum impurity models. *Phys. Rev. Lett.* **97**, 076405 (2006).
46. Zhou, K.-J. *et al.* I21: an advanced high-resolution resonant inelastic X-ray scattering beamline at Diamond Light Source. *J. Synchrotron Radiat.* **29**, 563–580 (2022).

Acknowledgements

We thank R. Comin, H. Luo, H. Weng, and E. Liu for insightful discussions. We also thank Y. Huang for the support on the samples. All data were taken at the I21 RIXS beamline of Diamond Light Source (United Kingdom) using the RIXS spectrometer designed, built and owned by Diamond Light Source. We thank Diamond Light Source for providing beam time under proposal ID NR27905. We acknowledge T. Rice for the technical support throughout the experiments. We also thank G. B. G. Stenning and D. W. Nye for help on the Laue instrument in the Materials Characterisation Laboratory at the ISIS Neutron and Muon Source. Z.Y. was supported by the NSFC (Grant No. 12074041 and 11674030) and the National Key Research and Development Program of China grant 2016YFA0302300. The calculations used high performance computing clusters at Beijing Normal University, China. H.C.L. was supported by National Key R&D Program of China (Grant No. 2018YFE0202600 and 2022YFA1403800), Beijing Natural Science Foundation (Grant No. Z200005), National Natural Science Foundation of China (Grant No. 12274459).

Author contributions

K.-J.Z. conceived the project. K.-J.Z. and A.N. supervised the project. A.N., K.-J.Z., J.L., S.A., H.C.R, M.G.-F., and A.C.W. performed RIXS measurements. A.N. and K.-J.Z. analysed RIXS data. Q.W., Q.W.Y. and H.C.L. synthesized and characterised the sample. Y.P. and Z.Y. performed DMFT calculations. A.N. and K.-J.Z. wrote the manuscript with comments from all the authors.

Competing interests

The Authors declare no competing interests.

Additional information

Supplementary Information is available for this paper.

Correspondence and requests for materials should be addressed to K.-J.Z. or A.N. or Z.Y.

Reprints and permissions information is available at www.nature.com/reprints

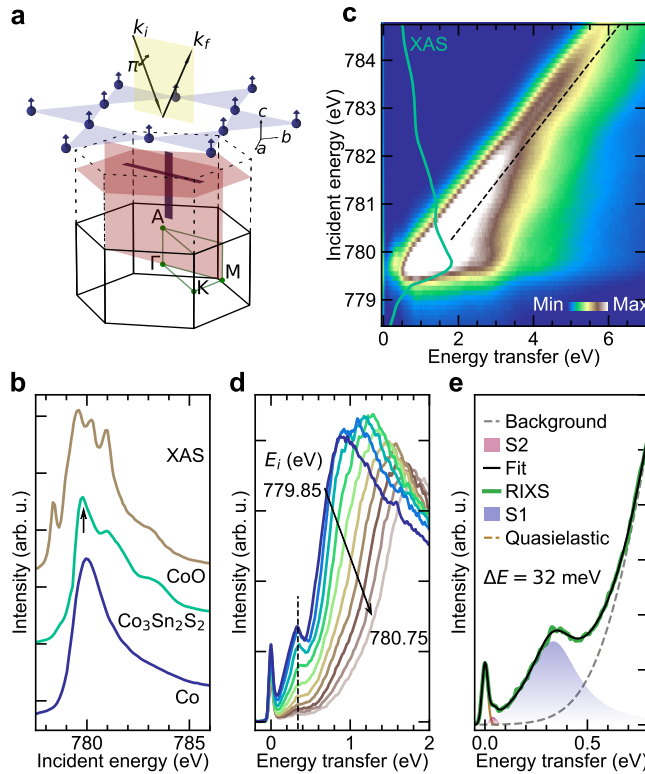


Figure 1. Spectroscopic signatures of correlated states in $\text{Co}_3\text{Sn}_2\text{S}_2$. **a**, Two dimensional (2D) FM Kagomé unit formed by Co atoms in $\text{Co}_3\text{Sn}_2\text{S}_2$ with the RIXS scattering geometry. The magnetic easy axis is along the crystallographic c -direction. RIXS measurements presented have been collected at the points shown by horizontally and vertically shaded strips parallel to Γ -M and Γ -A directions respectively. **b**, Comparison of multiplet features observed in the Co L_3 -edge XAS of CoO, $\text{Co}_3\text{Sn}_2\text{S}_2$ and Co metal shifted vertically. The arrow shows the E_i used for the momentum and temperature dependent RIXS measurements. **c**, RIXS map with E_i varied across the Co L_3 -edge on $\text{Co}_3\text{Sn}_2\text{S}_2$ at 23 K at $(-0.05, 1.60)$. The dashed line follows the main fluorescence feature. Co L_3 -edge XAS spectrum of $\text{Co}_3\text{Sn}_2\text{S}_2$ (green solid line) is superimposed on top of the RIXS map. **d**, RIXS line cuts from **c** above the Co L_3 -XAS threshold in steps of $\Delta E_i = 0.1$ eV. The vertical dashed line shows the E_i independent feature. **e**, Representative low-energy RIXS spectrum at $(0.1, 1.25)$ with aggregated least square fit of different low energy peak profiles and a high energy background. As discussed in the text, S1 and S2 primarily represent Stoner excitations from spin-polarised flatbands.

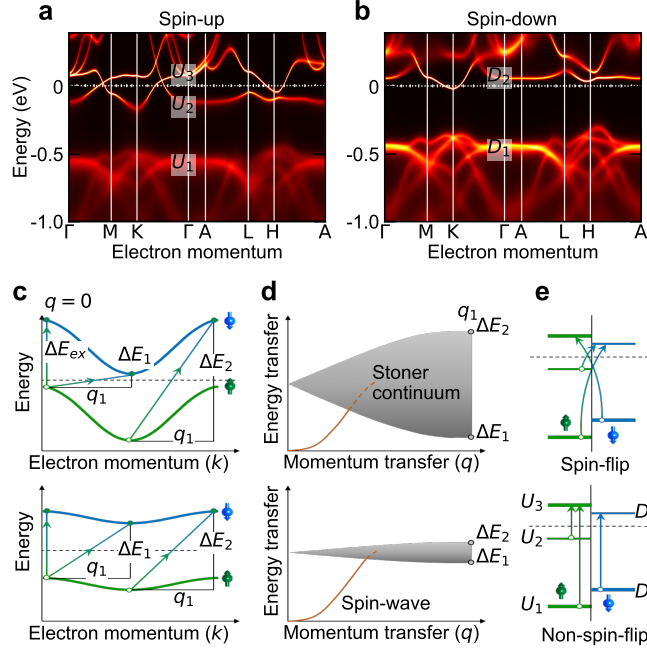


Figure 2. Flat band Stoner excitations in $\text{Co}_3\text{Sn}_2\text{S}_2$. Calculated spin-resolved electronic bands in $\text{Co}_3\text{Sn}_2\text{S}_2$ for the FM state with **a**, spin-up and **b**, spin-down bands. **c**, Schematic representation of electronic bands and spin-flip Stoner excitations comprising of electron-hole pairs of opposite spins, shown for zero ($\Delta k = q = 0$) and non-zero ($\Delta k = q_1 \neq 0$) momentum transfer values. For a rigid band splitting, $q = 0$ excitations have an energy equal to the exchange splitting as seen in panel **c**. For non-zero values of q , excitation pathways with different energies are satisfied giving rise to a continuum of excitations called the Stoner continuum spread across the $E - q$ -space ($\Delta E_2 \gg \Delta E_1$). **d**, Stoner continuum of excitations corresponding to the electronic bands shown in panel **c**. As the bands become flatter or dispersionless, the range of energies for these pathways reduces giving rise to a narrower band of excitations ($\Delta E_2 \simeq \Delta E_1$). **e**, Schematic spin-flip and non-spin-flip $q = 0$ excitations close to Γ , from and to the points marked in panels **a** and **b**.

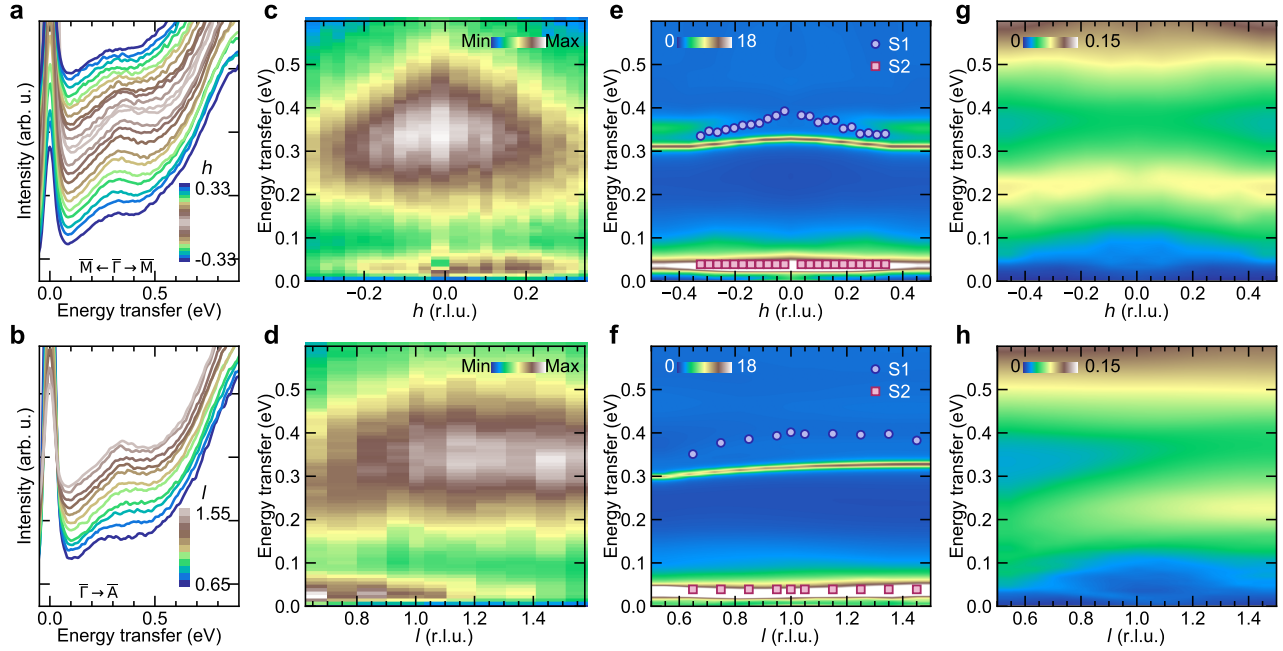


Figure 3. Dispersion of the flat band Stoner excitations in the $E - q$ -space in $\text{Co}_3\text{Sn}_2\text{S}_2$. RIXS line spectra for momentum transfer parallel to **A**, $\Gamma - \bar{M}$ direction from $h = -0.33$ to $h = 0.33$ at $l = 1.25$ and **B**, $\Gamma - \bar{A}$ direction from $l = 0.65$ to $l = 1.55$ at $h = 0.05$. **C**, **D**, RIXS intensity maps corresponding to the line spectra shown in **A**, **B**, with fitted elastic and background contributions subtracted. **E**, **F** Calculated vertex corrected dynamic spin structure factor $S(q, \omega)$ intensity maps along the RIXS measurement directions for spin-flip Stoner excitations. The markers are the ω_0 values of S1 and S2 peaks extracted from least square fits of RIXS spectra (see Methods). **G**, **H** Calculated vertex corrected dynamic charge structure factor intensity maps along the RIXS measurement directions for non-spin-flip charge excitations.

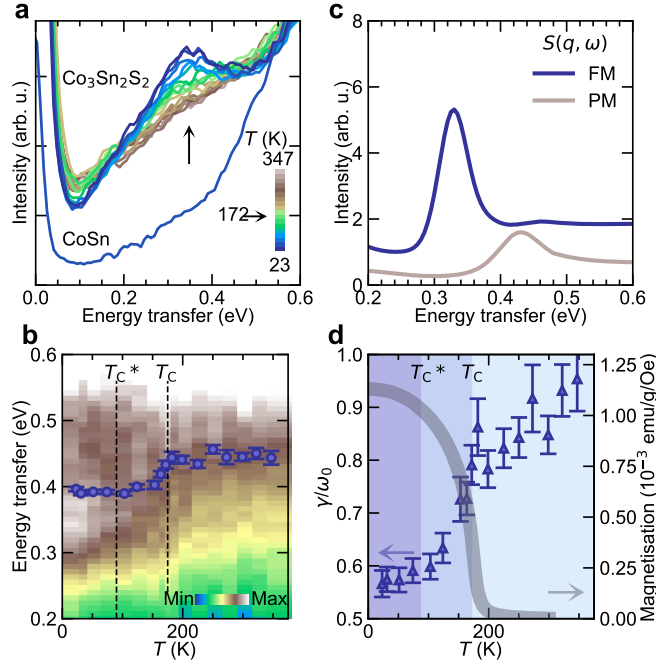


Figure 4. Temperature dependence of the flat band Stoner excitations in $\text{Co}_3\text{Sn}_2\text{S}_2$. Low energy RIXS spectra at $(0.025, 1.25)$ at temperatures ranging from 23 K to 347 K shown as **a**, lines and **b**, intensity map for $\text{Co}_3\text{Sn}_2\text{S}_2$. Also compared in panel **a** is the low energy RIXS spectra from paramagnetic flat band material CoSn at $(-0.15, 0.5)$ collected at 20 K. The markers in **b**, are the ω_0 values of S1 extracted from least square fits of RIXS spectra. **c**, Calculated $S(q, \omega)$ convoluted with the experimental resolution for the FM and the PM band configurations at $(0.025, 1.25)$. **d**, Extracted damping of S1 as a variation of temperature compared to the magnetisation data of $\text{Co}_3\text{Sn}_2\text{S}_2$. Shaded regions from 0-90 K, 90-175 K and 175-350 K represent c -axis FM, c -axis FM with ab -plane antiferromagnetic, and the PM magnetisation volume, respectively in $\text{Co}_3\text{Sn}_2\text{S}_2$ under zero-applied-field from Ref. ¹⁹ Error bars are least-square-fit errors

Supplementary Information for Correlation driven near-flat band Stoner excitations in a Kagome magnet

Abhishek Nag^{1,*}, Yiran Peng², Jiemin Li^{1,3}, S. Agrestini¹, H. C. Roberts^{1,4}, Mirian García-Fernández¹, A. C. Walters¹, Qi Wang⁵, Qiangwei Yin⁵, Hechang Lei⁵, Zhiping Yin^{2,†}, and Ke-Jin Zhou^{1,‡}

¹Diamond Light Source, Harwell Campus, Didcot OX11 0DE, United Kingdom

²Department of Physics and Center for Advanced Quantum Studies, Beijing Normal University, Beijing 100875, China

³Beijing National Laboratory for Condensed Matter Physics and Institute of Physics, Chinese Academy of Sciences, Beijing 100190, China

⁴H. H. Wills Physics Laboratory, University of Bristol, Bristol BS8 1TL, United Kingdom

⁵Department of Physics and Beijing Key Laboratory of Opto-Electronic Functional Materials & Micro-Nano Devices, Renmin University of China, Beijing, China

*e-mail: abhishek.nag@diamond.ac.uk

†e-mail: yinzhiping@bnu.edu.cn

‡e-mail: kejin.zhou@diamond.ac.uk

S1 Sample information

$\text{Co}_3\text{Sn}_2\text{S}_2$ single crystal grown by the Sn flux method and used for the RIXS measurements is shown in Fig. **S1a**. The X-ray diffraction (XRD) peaks of the single crystal were measured using a Bruker D8 X-ray machine with $\text{Cu } K_\alpha$ radiation ($\lambda = 0.15418$ nm) at room temperature (Fig. **S1b**). All of the peaks can be indexed by the indices of $(0, 0, l)$ lattice planes. It shows that the crystal surface is normal to the c -axis with the plate-shaped surface parallel to the ab plane. Fig. **S1c** shows the Laue diffraction pattern obtained from the single crystal at room temperature. Fig. **S1d** shows the Zero-Field-Cooled (ZFC) and Field-Cooled (FC) magnetisation data obtained as a variation of temperature under an applied magnetic field of 1 T along the c -axis. Ferromagnetic (FM) transition temperature T_C from magnetisation measurements was found to be 172 K. The inset shows magnetisation data obtained as a variation of magnetic field applied along the c -axis at 5 and 300 K.

S2 RIXS data fitting

RIXS data were fitted as described in Methods of main text. The RIXS line spectra and their fits are shown in panels a and b of Fig. S2, Fig. S3 and Fig. S4. The quasielastic peaks at zero energy transfer have been subtracted by fitting a Gaussian lineshape matching the experimental energy resolution, for better visualisation of the low energy peak S2. Due to the large damping factors of the peak S1 as shown in panel c of Fig. S2, Fig. S3 and Fig. S4, the associated undamped peak energies as shown in panel d of Fig. S2, Fig. S3 and Fig. S4, are higher than the peak maximum energies.

S3 High resolution RIXS data

Higher resolution ($\Delta E = 32$ meV) RIXS spectra were collected at Co L_3 -edge to separate the quasielastic peak contribution from the low energy S2 peak as shown in Fig. S6, for both π (incident polarisation of X-ray parallel to the scattering plane) and σ (incident polarisation of X-ray perpendicular to the scattering plane). Both the quasielastic peak and S2 at ~ 0.04 eV show marginally higher intensity with the π polarisation for all (h, l) points.

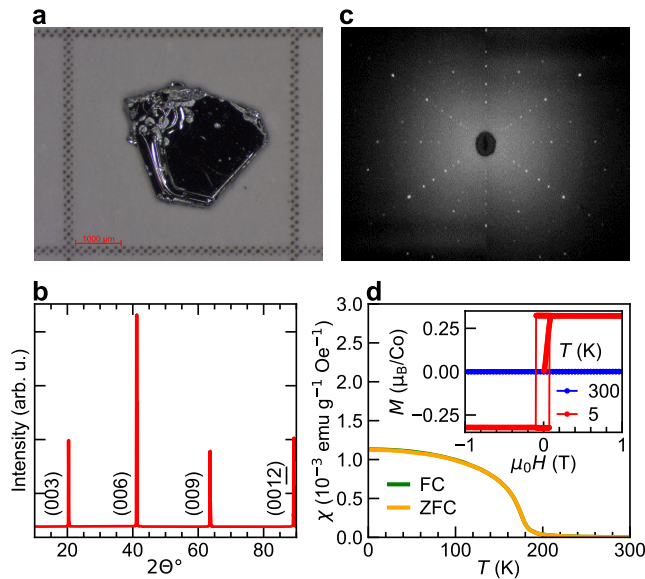


Figure S1. $\text{Co}_3\text{Sn}_2\text{S}_2$ sample characterisation. **a**, Photograph of a single crystal of $\text{Co}_3\text{Sn}_2\text{S}_2$. **b**, XRD peaks of the $\text{Co}_3\text{Sn}_2\text{S}_2$ single crystal. **c**, Laue diffraction pattern of the $\text{Co}_3\text{Sn}_2\text{S}_2$ single crystal. **d**, ZFC-FC data magnetisation data of $\text{Co}_3\text{Sn}_2\text{S}_2$ single crystal with magnetic field of 1 T applied along the c -axis. Inset shows magnetisation data obtained as a variation of magnetic field applied along the c -axis at 5 and 300 K.

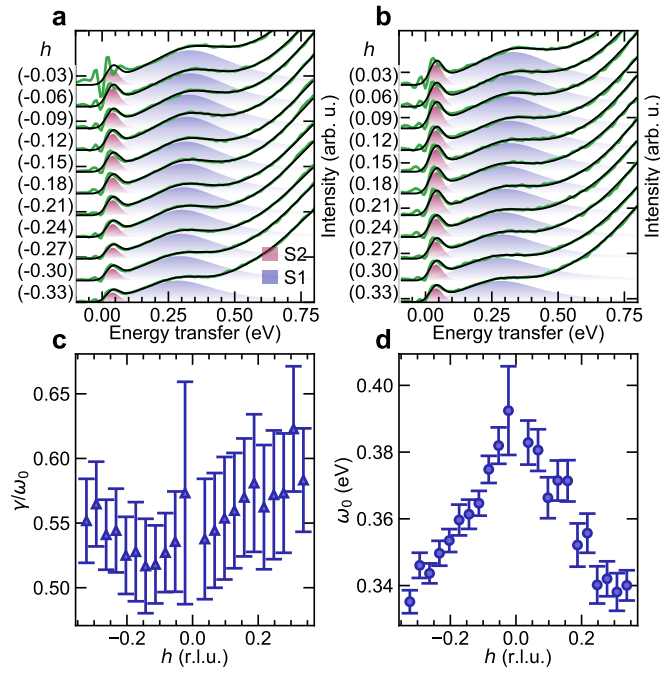


Figure S2. h -dependent RIXS spectra of $\text{Co}_3\text{Sn}_2\text{S}_2$ at 23 K with fitting. **a, b,** Low-energy RIXS spectra (green lines) along $\overline{M}\overline{\Gamma}\overline{M}$ direction for $h = -0.33$ to $h = 0.33$ at $l = 1.25$. The fitted quasielastic peak contributions have been subtracted. Black lines are aggregated least square fits of different low energy peak profiles and a high energy background. The shaded peak profiles S1 and S2 primarily represent Stoner excitations from spin-polarised flatbands. **c,** The damping factor and **d,** the undamped energy ω_0 of S1, extracted from fits of the RIXS spectra. Error bars are least-square-fit errors.

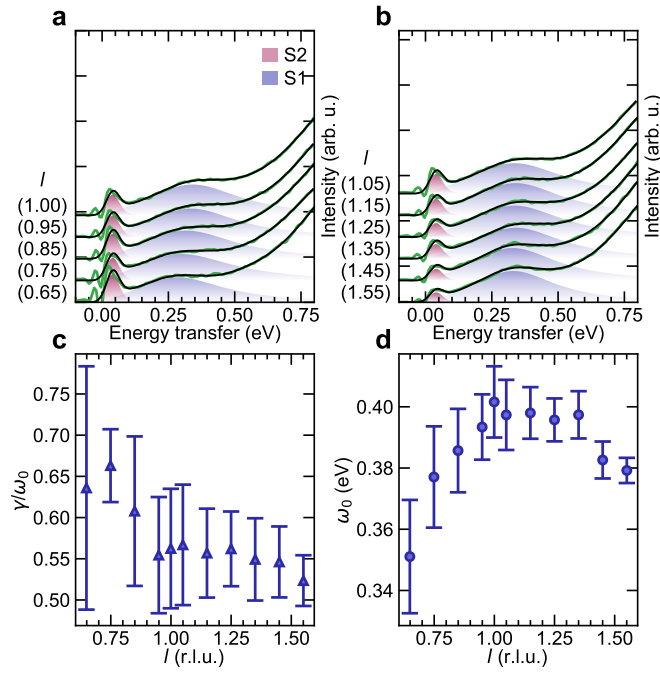


Figure S3. l -dependent RIXS spectra of $\text{Co}_3\text{Sn}_2\text{S}_2$ at 23 K with fitting. **a, b,** Low-energy RIXS spectra (green lines) along $\bar{\Gamma}-\bar{A}$ direction for $l = 0.65$ to $l = 1.55$ at $h = 0.05$. The fitted quasielastic peak contributions have been subtracted. Black lines are aggregated least square fits of different low energy peak profiles and a high energy background. The shaded peak profiles S1 and S2 primarily represent Stoner excitations from spin-polarised flatbands. **c,** The damping factor and **d,** the undamped energy ω_0 of S1, extracted from fits of the RIXS spectra. Error bars are least-square-fit errors.

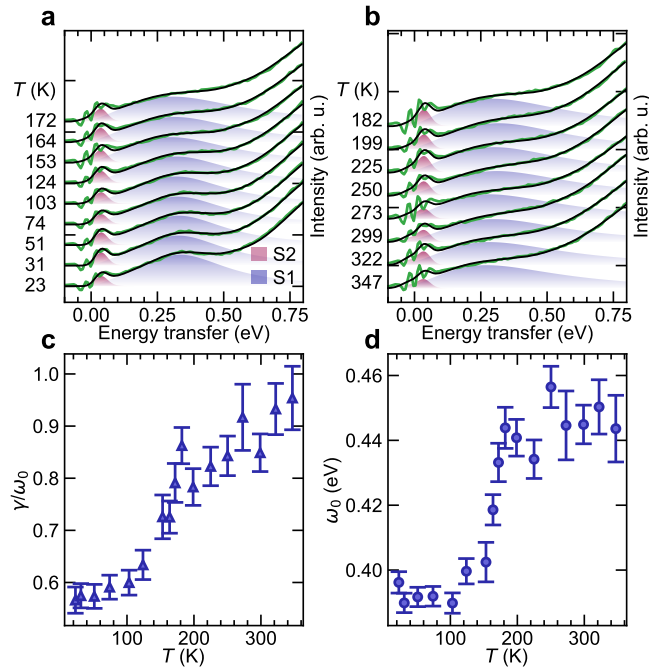


Figure S4. Temperature dependent RIXS spectra of $\text{Co}_3\text{Sn}_2\text{S}_2$ at $(0.025, 1.25)$ with fitting. **a, b**, Low-energy RIXS spectra (green lines) for different temperatures. The fitted quasielastic peak contributions have been subtracted. Black lines are aggregated least square fits of different low energy peak profiles and a high energy background. The shaded peak profiles S1 and S2 primarily represent Stoner excitations from spin-polarised flatbands. **c**, The damping factor and **d**, the undamped energy ω_0 of S1, extracted from fits of the RIXS spectra. Error bars are least-square-fit errors.

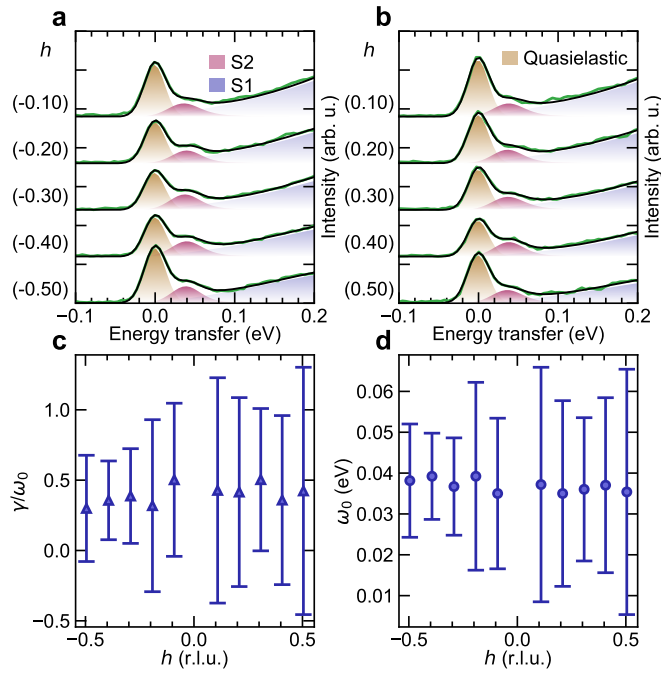


Figure S5. Low-energy high energy resolution RIXS spectra of $\text{Co}_3\text{Sn}_2\text{S}_2$ at 23 K with fitting. **a, b,** RIXS spectra highlighting the S2 peaks (green lines). Black lines are aggregated least square fits of different low energy peak profiles and a high energy background. The shaded peak profiles S1 and S2 primarily represent Stoner excitations from spin-polarised flatbands. **c,** The damping factor and **d,** the undamped energy ω_0 of S2, extracted from fits of the RIXS spectra. Error bars are least-square-fit errors.

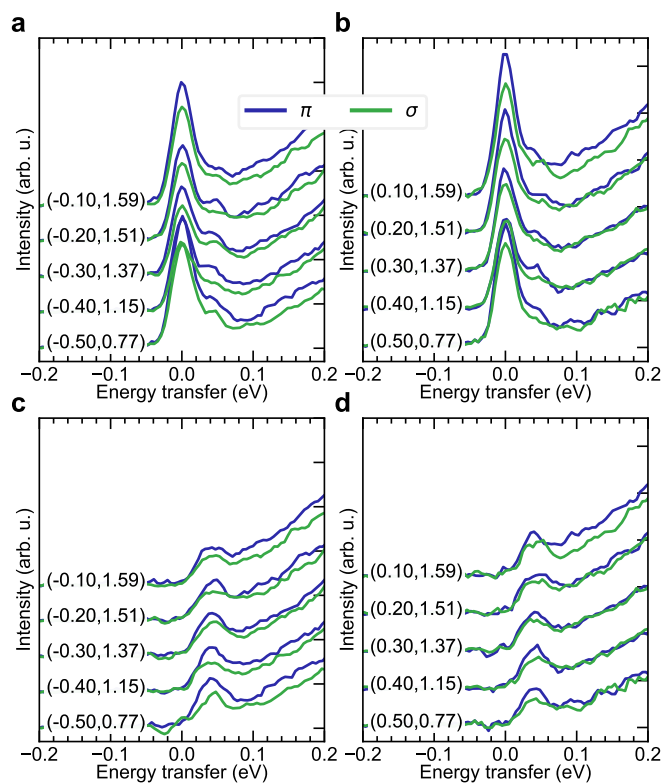


Figure S6. Polarisation dependent high energy resolution RIXS spectra of $\text{Co}_3\text{Sn}_2\text{S}_2$ at 23 K. **a, b,** High resolution ($\Delta E = 32$ meV) RIXS spectra on $\text{Co}_3\text{Sn}_2\text{S}_2$ collected with π and σ incident polarisations of X-ray. **c, d,** Same spectra with the fitted quasielastic peak contributions subtracted.

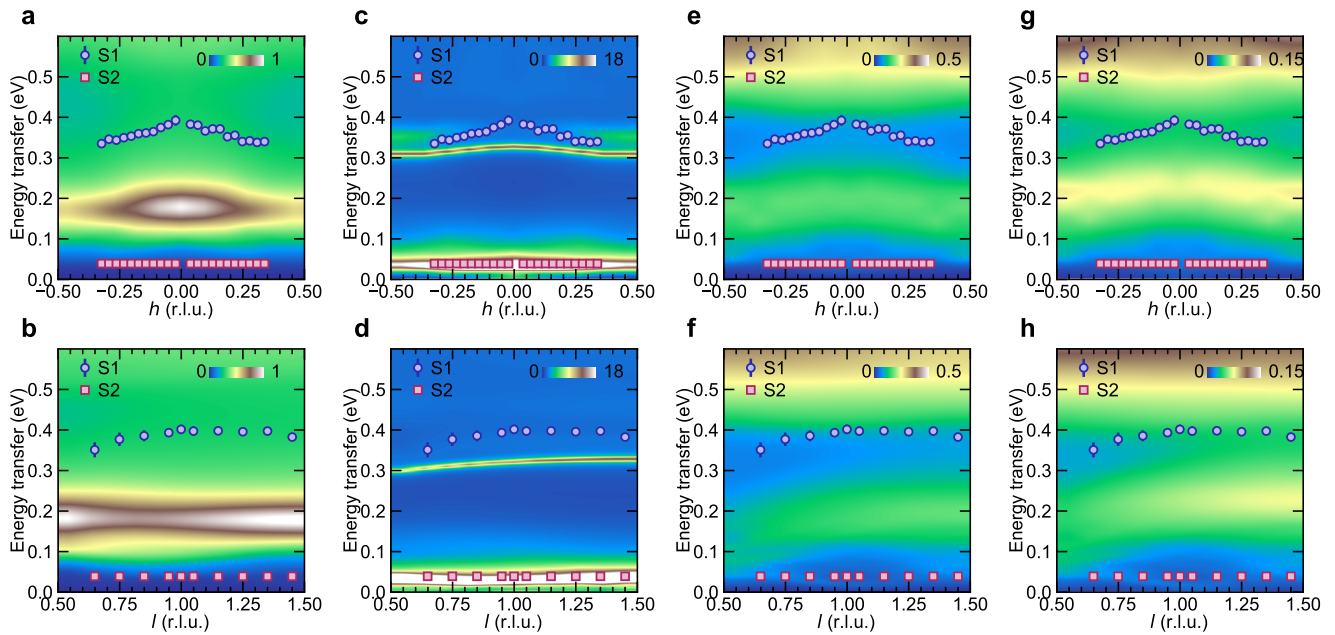


Figure S7. Calculated dynamic spin and charge susceptibilities in $\text{Co}_3\text{Sn}_2\text{S}_2$. Bare spin susceptibility intensity maps along the $\bar{M}\bar{\Gamma}\bar{M}$ and **b**, $\bar{\Gamma}\bar{A}$ directions. Vertex corrected spin structure factor intensity maps along the **c**, $\bar{M}\bar{\Gamma}\bar{M}$ and **d**, $\bar{\Gamma}\bar{A}$ directions. Bare charge susceptibility intensity maps along the **e**, $\bar{M}\bar{\Gamma}\bar{M}$ and **f**, $\bar{\Gamma}\bar{A}$ directions. Vertex corrected charge susceptibility intensity maps along the **g**, $\bar{M}\bar{\Gamma}\bar{M}$ and **h**, $\bar{\Gamma}\bar{A}$ directions. The markers are the ω_0 values of S1 and S2 peaks extracted from least square fits of RIXS spectra. Error bars are least-square-fit errors.

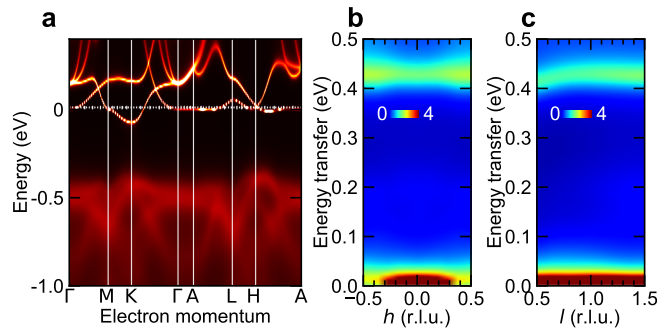


Figure S8. Paramagnetic state of $\text{Co}_3\text{Sn}_2\text{S}_2$. **a**, Calculated electronic bands in $\text{Co}_3\text{Sn}_2\text{S}_2$ in the paramagnetic state. Vertex corrected spin structure factor intensity maps along the **b**, $\bar{M}\bar{\Gamma}\bar{M}$ and **c**, $\bar{\Gamma}\bar{A}$ directions in the paramagnetic state.

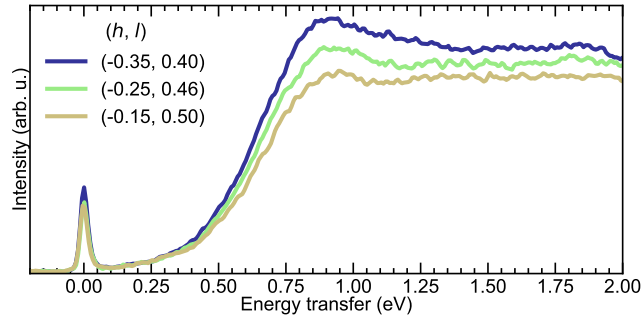


Figure S9. RIXS spectra of CoSn. Co L_3 -edge RIXS spectra collected on paramagnetic flat band material CoSn at 20 K at different (h, l) points with σ polarisation.

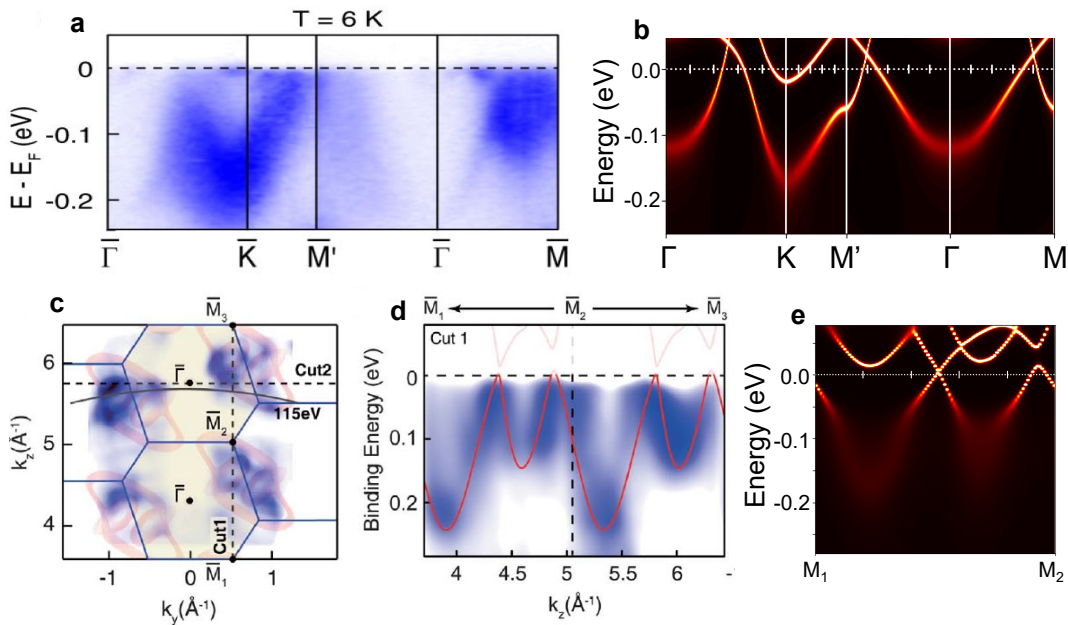


Figure S10. Comparison of ARPES data on $\text{Co}_3\text{Sn}_2\text{S}_2$ with band structure calculations. **a**, ARPES intensity plot along $\bar{\Gamma}-\bar{K}-\bar{M}'-\bar{\Gamma}-\bar{M}$, reprinted figure with permission from D. F. Liu *et al.*, Topological phase transition in a magnetic weyl semimetal, Phys. Rev. B, **104**, 205140 (2021). Copyright (2021) by the American Physical Society. **b**, Calculated electronic bands for the ferromagnetic state along $\bar{\Gamma}-\bar{K}-\bar{M}'-\bar{\Gamma}-\bar{M}$ using DFT+DMFT in the present work. **c**, ARPES intensity plot along k_y - k_z plane with energy integration window from $E_F-0.1$ eV to E_F from from Liu *et al.* The black curve indicates the k_z momentum locations probed by 115-eV photons. The dashed line marked as 'cut1' indicates the momentum direction $\bar{M}_1-\bar{M}_2-\bar{M}_3$ of the ARPES data shown in panel **d** from D. F. Liu *et al.*, Magnetic Weyl semimetal phase in a Kagomé crystal, Science, **365**, 1282-1285 (2019). Reprinted with permission from AAAS. The red curves in panel **d** are from DFT calculations, where the calculated bandwidth was renormalised by a factor of 1.43 and the energy position was shifted to match the experiment. **e** Calculated electronic bands for the ferromagnetic state along $\bar{M}_1-\bar{M}_2$ using DFT+DMFT in the present work.